Research Square

Preprints are preliminary reports that have not undergone peer review.
They should not be considered conclusive, used to inform clinical practice,
or referenced by the media as validated information.

Tropical forest loss causes observed reductions in downwind tropical precipitation

Edward Butt

E.Butt@leeds.ac.uk

University of Leeds https://orcid.org/0000-0002-6087-4848

Callum Smith

University of Leeds https://orcid.org/0000-0002-2705-8398

Jessica Baker

University of Leeds https://orcid.org/0000-0002-3720-4758

Stephen Arnold

University of Leeds

Murilo Lemes

National Institute for Space Research: Instituto Nacional de Pesquisas Espaciais

Gilvan Sampaio

Center for Earth System Science (CCST), National Institute For Space Research (INPE)

Dominick Spracklen

Institute for Climate and Atmospheric Science https://orcid.org/0000-0002-7551-4597

Physical Sciences - Article

Keywords:

Posted Date: May 14th, 2026

DOI: https://doi.org/10.21203/rs.3.rs-9584800/v1

License: This work is licensed under a Creative Commons Attribution 4.0 International License.
Read Full License

Additional Declarations: There is **NO** Competing Interest.

Tropical forest loss causes observed reductions in downwind tropical precipitation

Edward W. Butt[1*], Callum Smith[1], Jessica C. A. Baker[1], Steve R. Arnold[1], Murilo R. Lemes[2], Gilvan Sampaio[2] and Dominick V. Spracklen[1]

[1]*School of Earth and Environment, University of Leeds, Leeds, UK*

[2]*National Institute for Space Research: Instituto Nacional de Pesquisas Espaciais, São José dos Campos, State of São Paulo, Brazil*

*Correspondence to Edward W. Butt: e.butt@leeds.ac.uk

Abstract

Tropical forests regulate regional rainfall through evapotranspiration and atmospheric moisture recycling, yet the extent to which recent deforestation has contributed to downwind precipitation declines remains uncertain. Here we combine satellite precipitation and forest-loss observations with Lagrangian air-mass back-trajectory analysis to quantify how exposure to upwind deforestation is associated with rainfall trends across the tropics (30°S–30°N) from 2001 to 2024. Increasing air-mass exposure to forest loss over the preceding 1–10 days is consistently associated with more negative trends in annual, wet-season and dry-season precipitation. Across the tropics, regions experiencing the largest increases in 5-day air-mass exposure to upwind forest loss exhibit precipitation trends 23.8 ± 1.4 mm yr^{-1} per year more negative than regions with the smallest exposure changes. Sustained over the study period, this corresponds to 572 ± 33 mm lower annual precipitation, equivalent to a shift of more than three standard deviations relative to interannual variability. Machine-learning models trained on air-mass pathway variables identify exposure to forest loss as the dominant predictor of long-term precipitation change, exceeding the influence of ocean surface temperature, land surface temperature, transport distance and elevation along back trajectories. The strongest associations occur across tropical South America, particularly southern Brazil and Peru, and across sub-Saharan Africa. Together, these results provide observational evidence that recent deforestation has weakened regional moisture recycling across the tropics and driven

substantial, persistent declines in downwind precipitation through multi-day atmospheric transport pathways.

Main

Tropical deforestation alters local and regional climate, leading to local [1] and regional [2] warming and altering local precipitation [3]. Warming from tropical deforestation negatively impacts outdoor workers [4] and increases heat-related mortality [5]. Reductions in rainfall reduce crop yields [6,7] and forest carbon sink [8], increase fire risk [9], reduce hydropower generation [10] and restrict river transport [11]. Understanding the local and regional climate impacts of deforestation is crucial to inform sustainable land-use policy across the tropics.

Tropical forests emit large quantities of water to the atmosphere via evapotranspiration (ET) and this plays a critical role in sustaining regional rainfall [12]. ET from tropical forests accounts for up to 25% - 40% of rainfall across the Amazon (Baker & Spracklen, 2022; Dominguez et al., 2022). In some catchments, such as Río de la Plata in South America, forest-derived moisture may account for as much as 70% of rainfall [15]. Atmospheric transport modelling shows that air masses trajectories passing over densely forested regions produce significantly more precipitation than those traveling over sparsely vegetated areas—likely reflecting the enhanced moisture input via ET from forested landscapes [12]. Recycled moisture can help buffer the effects of drought [16], while successive ET–rainfall cycles can increase rainfall far from oceanic moisture sources [17].

Despite this growing body of evidence on the links between tropical forests and rainfall, the impacts of tropical deforestation on regional and downwind rainfall are still uncertain. Climate models predict that tropical deforestation reduces regional rainfall, but with large inter-model variability [18–20]. Some high-resolution models, including convection permitting models, predict deforestation causes little change in precipitation [21]. Datasets of observed deforestation and precipitation over the past few decades provide an opportunity to explore links between forest loss and rainfall. Reductions in precipitation have been observed over regions of tropical forest loss [3] and observed declines in dry season precipitation in the Brazilian legal Amazon have been linked to local deforestation [22,23]. Crucially, an assessment of observed rainfall trends across the tropics and whether they are causally linked to upwind deforestation is lacking.

Here we present the first pantropical analysis of the association between atmospheric exposure to tropical deforestation between 2001 and 2024 and observed trends in tropical rainfall. We combined satellite-based forest cover and forest loss data with atmospheric back-trajectory

modelling to quantify cumulative exposure of air parcels to deforested areas. We run back trajectories arriving at every 1° × 1° tropical land grid cell location every 6 hours over the 2001 to 2024 period, which equates to approximately 600 million trajectories. This allows us to track how exposure to forest loss has changed over this period, accounting for both changes in forest loss and changes in atmospheric circulation. Satellite-derived precipitation datasets were used to evaluate observed trends in rainfall. We evaluated whether increased exposure to deforested areas was associated with observed reductions in precipitation.

Figure 1 shows spatial patterns of forest loss across the tropics (30°S–30°N) for 2001–2024. Extensive deforestation is concentrated in the southern Amazon, the Chaco region of southern Brazil and Paraguay, and parts of sub-Saharan Africa and Southeast Asia, with local forest loss in some regions exceeding 15 percentage points (Fig. 1a).

We used a Lagrangian atmospheric transport model to simulate atmospheric transport patterns and air mass exposure to forest loss (see Methods). Five-day cumulative exposure to forest loss exceeds 100 %-point day and extends well beyond deforested regions, with pronounced signals downwind of the southern Amazon across southern Brazil (~80 %-point day) and of the Congo (Fig. 1b). Exposure to forest loss along shorter back trajectories (1 day) more closely reflects local-scale forest loss, whereas exposure increases and spatial patterns stabilise across longer multi-day back trajectories (Supplementary Fig. S1).

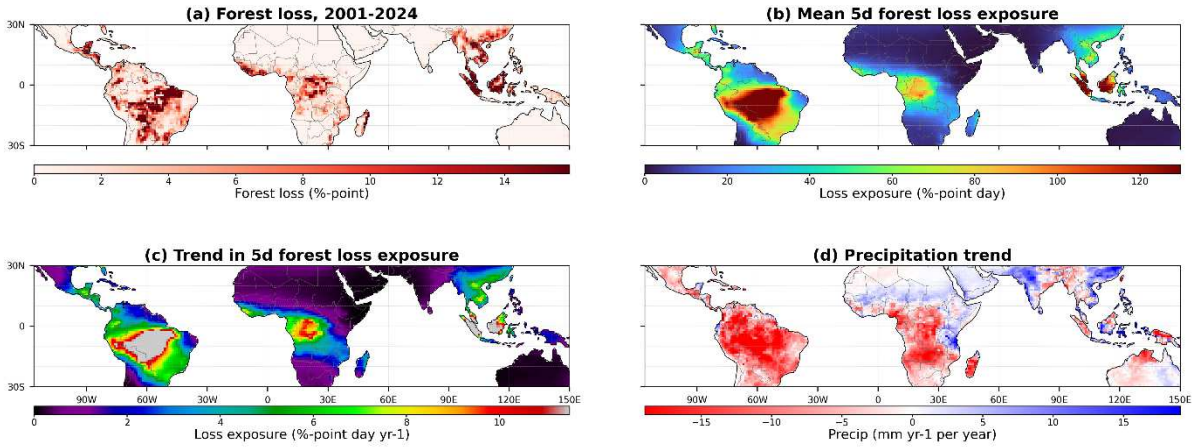


Figure 1. Forest loss and rainfall trends over 2001 to 2024. *(a) Forest percentage-point loss (b) Annual mean 5-day (5d) cumulative air mass exposure to forest loss, (c) Trend in annual mean 5-d cumulative air mass exposure to forest loss, (d) Trend in annual rainfall calculated as the average of six satellite datasets. Forest loss data in (a-c) is from GFC.*

The 2001–2024 trend in preceding 5-d cumulative air mass exposure to forest loss (Fig. 1c) identifies regions where air parcels have increasingly traversed deforested landscapes over the 24-year period. Positive trends in exposure are widespread across the tropics, with large annual increases exceeding 10 %-point day yr^{-1} evident downwind of deforested regions, including the southern Amazon, the Congo Basin, and Borneo (Fig. 1c). The strengthening of exposure is consistent across alternative exposure windows (1 to 10 days), with shorter windows showing more localised signals and longer windows yielding larger but spatially coherent increases (Supplementary Fig. S2).

To account for spatial differences in baseline forest loss exposure and climate variability, we also explored trends relative to local interannual variability (standard deviations (SD) yr^{-1}) (Supplementary Fig. S3). Relative increases exceeding 0.14 SD yr^{-1} occur downwind of deforested regions (Supplementary Fig. S3c). Sustained over 24 years, trends of this magnitude result in an end-of-period shift exceeding three standard deviations.

There is large spatial and temporal variability in tropical precipitation over the past few decades [24,25] with diverse representation in different datasets. To provide the most robust representation of recent trends we used an ensemble of six precipitation datasets (see Methods). Reductions in precipitation over 2001–2024 exceeding 20 mm yr^{-1} per year are observed across southern and central Amazonia, southwestern Brazil, parts of the Congo Basin, Angola and Zambia and southern Madagascar (Fig. 1d). Trends in precipitation are substantial with respect to interannual variability for these same regions exceeding -0.1 SD yr^{-1}, equivalent to an end-of-period shift exceeding two standard deviations (Supplementary Figure S3d).

Reduced rainfall over this period has been previously reported in the Amazon [9,26,27] and the Congo Basin (Jiang et al., 2019; Raghavendra et al., 2020; Fu and Wu, 2024). Trends in tropical precipitation are caused by a wide variety of factors including decadal-scale modes of climate variability, increasing greenhouse gases and climate change, as well as changes in the land surface (Gu et al., 2016; Song et al., 2023). Climate mode adjusted precipitation trends (see Methods) closely mirror the observed trends in both spatial pattern and magnitude (Supplementary Fig. S4), indicating that the observed drying signals are not dominated by large-scale modes such as the El Niño–Southern Oscillation (ENSO), the Indian Ocean Dipole (IOD), or Atlantic Niño variability (ATL3).

Overall, regions exhibiting declining precipitation (Figure 1d; Supplementary Fig. S3d) largely overlap with areas where air masses have experienced increasing upwind exposure to forest

loss (Figure 1c; Supplementary Fig. S3c), consistent with a linkage between upwind deforestation and reduced rainfall.

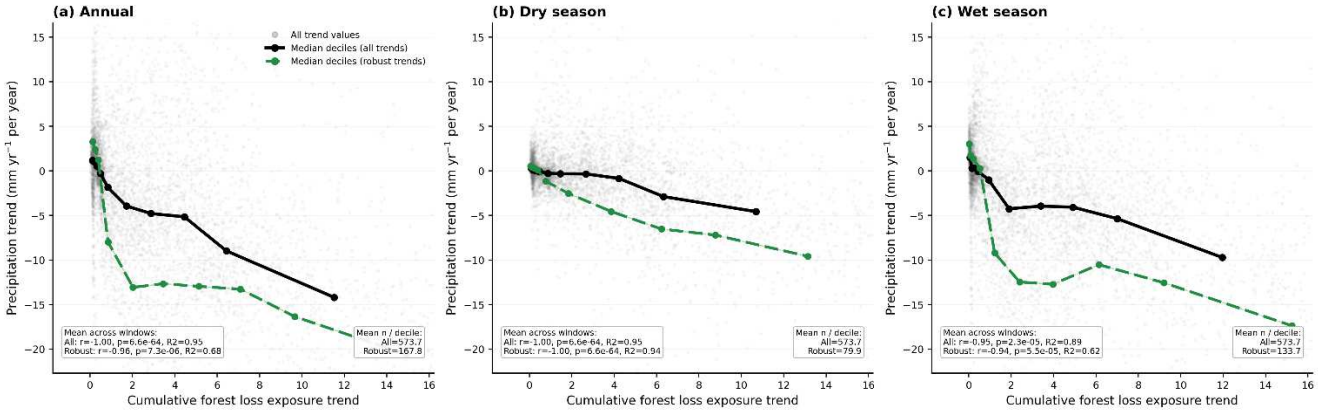


Figure 2. Relationship between 5-day cumulative forest-loss exposure trends and precipitation trends across the tropics. *Precipitation trends (mm yr $^{-1}$ per year) are shown as a function of trends in 5-day cumulative forest loss exposure along air-mass trajectories (%-point day yr $^{-1}$) for annual (a), dry-season (b) and wet-season (c). Grey points show trends for all tropical grid cells. Black lines show median precipitation trends across deciles of forest loss exposure trends for all grid cells, and dashed green lines show the corresponding relationship when restricted to grid cells with robust precipitation trends. Insets within panels report summary statistics for the median decile relationships, including Spearman correlation (r), significance (p), and coefficient of determination (R^2), alongside the mean number of samples (n) per decile.*

We explored this potential relationship between changes in upwind air mass exposure to forest loss and trends in precipitation. We find that regions with positive trends in 5-day cumulative air mass exposure to forest loss are strongly associated with more negative annual precipitation trends across the tropics (Fig. 2; Spearman's r = –1, p = 6.6×10^{-64}, R^2 = 0.95). Restricting the analysis to grid cell locations exhibiting statistically robust precipitation trends (see Methods) yields similarly strong annual associations (r = –0.96, p = 7.3×10^{-6}, R^2 = 0.68, n=~168 per decile). Similar relationships occur in the dry season (r = –1, p = 6.6×10^{-64}, R^2 = 0.94, n=~80 per decile), and in the wet season (r = –0.94, p = 5.5×10^{-5}, R^2 = 0.62, n=~134 per decile). The relationship between exposure to forest loss and precipitation is roughly linear which might be expected if reductions in precipitation are mainly driven by reduced precipitation recycling. However, our analysis does not preclude the potential for future tipping points where sharp reductions in precipitation might occur at greater exposure to forest loss than experienced in our 24-year observational record.

Stratifying robust precipitation trends by deciles of upwind forest loss exposure reveals progressively larger precipitation declines with increasing exposure. Locations in the highest

exposure decile exhibit pronounced negative precipitation trends annually (median = –20.6 (95% CI –36.2 to –12.0) mm yr^{-1} per year), in the dry-season (median = –9.6 (95% CI –16.8 to 18.0) mm yr^{-1} per year), and wet-season rainfall (–17.4 (95% CI –28.7 to –9.5) mm yr^{-1} per year). Expressed relative to local interannual variability, the same relationships remain significant (annual: r = –0.81, p = 0.005, R^2 = 0.79; dry season: r = –0.98, p = 1.5×10^{-6}, R^2 = 0.74; wet season r = –0.99, p = 9.3×10^{-8}, R^2 = 0.76; Supplementary Fig. S5). The highest exposure decile experiences relative annual declines of –0.08 (95% CI –0.12 to –0.05) SD yr^{-1}, with comparable reductions in the dry (–0.068 SD yr^{-1}) and wet seasons (–0.075 SD yr^{-1}).

The contrast in precipitation trends between regions with the greatest and smallest changes in forest loss exposure is substantial. Regions in the lowest exposure decile show weakly positive precipitation trends (annual median = +3.3 mm yr^{-1} per year; +0.07 SD yr^{-1}), whereas regions in the highest decile experience strong declines. The difference between upwind exposure extremes corresponds to regions with the greatest trend in forest loss exposure experiencing precipitation trends that are 23.8 ± 1.4 mm yr^{-1} per year (0.15 ± 0.06 SD yr^{-1}) more negative that regions with the smallest exposure trend. Sustained over the study period (2001–2024), annual precipitation in regions with the greatest increase in exposure to forest loss was 572 ± 33 mm lower than in regions with the lowest increases in exposure to forest loss, equivalent to more than three standard deviations in annual precipitation (-3.6 ± 0.13 SD). Seasonal contrasts are similarly pronounced. By 2024, dry season precipitation in regions of greatest increase in upwind forest loss exposure was 244 ± 25 mm lower (3.16 ± 0.12 SD), and wet season precipitation was 489 ± 28 mm lower (3.64 ± 0.13 SD) than in regions with the lowest increase in forest loss exposure. This indicates that precipitation downwind of extensive deforestation has shifted well beyond its typical interannual variability, reflecting a persistent and systematic alteration of the precipitation regime.

The consistency of the signal in both absolute (mm yr^{-1} per year) and standardised relative (SD yr^{-1}) units demonstrates that the association is not driven by baseline differences in precipitation magnitude but instead reflects a robust and spatially coherent link between increasing exposure to forest loss and declining precipitation across the tropics.

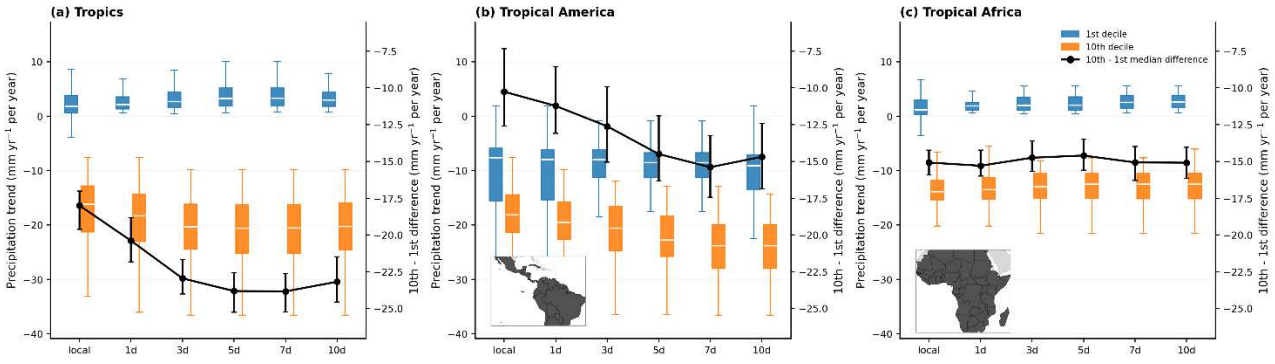


Figure 3. Annual rainfall trends downwind of low and high forest-loss exposure. *Distributions of robust trends in annual precipitation (2001–2024) in the lowest and highest deciles of local forest loss and cumulative upwind forest-loss exposure across (a) tropics (30°S–30°N), (b) tropical America, and (c) tropical Africa. Blue and orange boxes denote the 1st and 10th exposure deciles, respectively, across local loss (within the same grid cell) and 1–10 day upwind air-mass exposure to forest loss. Black points and lines show the median difference between the 10th and 1st deciles, with error bars indicating 95% confidence intervals, plotted against the right-hand y axis. Differences between decile distributions were estimated using a nonparametric bootstrap of resampled means to derive empirical 95% confidence intervals.*

To assess whether increasing exposure to forest loss is associated with systematically different precipitation trends, we compared annual precipitation trends between locations in the lowest (1st decile) and highest (10th decile) trend in exposure to forest loss. We completed this analysis at both the local and the regional scales. The local scale is calculated as the change in precipitation directly over regions of forest loss and is calculated at individual 1° × 1° grid cells representing scales of ≤ 100 km. The regional scale is calculated from upwind cumulative forest-loss exposure along air-mass back trajectories over the preceding 1–10 days, representing average transport distances of approximately 500 to 5000 km (Fig. 3). This framework distinguishes local land–atmosphere effects from regional moisture-transport pathways.

Across the tropics (Fig. 3a), locations in the highest decile of increased exposure to forest loss consistently exhibit more negative annual precipitation trends than those in the lowest decile. Regions experiencing the greatest increase in local forest loss exposure show negative rainfall trends, consistent with recent evidence for local rainfall suppression following forest loss [3]. However, the contrast strengthens when forest loss is measured along air-mass pathways. The difference between the 1st and 10th decile distributions is largest for 5–7 day back trajectories, representing regional transport over several thousand kilometres. For 5-day back trajectories,

locations with the smallest increases in forest-loss exposure show weakly positive annual precipitation trends (median = +3.3 mm yr^{-1} per year), whereas locations with the greatest increase in forest-loss exposure exhibit pronounced declines (median = -20.6 mm yr^{-1} per year). This corresponds to precipitation trends that are 23.8 ± 1.4 mm yr^{-1} per year more negative in the highest exposure decile than in the lowest exposure decile, equivalent to 572 ± 33 mm lower annual rainfall by the end of the study period. The 7-day contrast is similar (-23.8 ± 1.3 mm yr^{-1} per year; 572 ± 31 mm by study end). These regional-scale contrasts exceed the local contrast (-18 ± 1.3 mm yr^{-1} per year), indicating that the influence of forest loss extends beyond local land–atmosphere coupling.

Regionally consistent patterns emerge in tropical America (Fig. 3b) and tropical Africa (Fig. 3c). Across tropical America, precipitation trends are negative across both deciles, but reductions are substantially stronger in the decile of greatest exposure increase. For 5–10 day back trajectories, median differences range from -14.5 ± 2.2 to -15.4 ± 2.1 mm yr^{-1} per year, corresponding to 348 ± 53 to 369 ± 50 mm lower annual rainfall by 2024 in regions with the greatest increase in forest-loss exposure. In tropical Africa, regions with the smallest increase in forest-loss exposure exhibit positive precipitation trends, whereas regions with the greatest increase in exposure show strong precipitation declines. Across 5–10 day back trajectories, median annual contrasts remain close to -15 mm yr^{-1} per year, corresponding to approximately 350–362 mm lower annual rainfall by the end of the study period. In both regions, precipitation declines more strongly downwind of forest loss than directly above forest loss, suggesting that reductions in multi-day air-mass accumulation of moisture at regional scales are a key driver of rainfall decline. Across tropical America, declines strengthen from local to multi-day exposure windows and peak around 7 days, supporting a cumulative role for weakened moisture recycling across the continent downwind of forest loss.

To account for spatial differences in baseline rainfall variability, we repeated this analysis using standardised relative trends (SD yr^{-1}) (Supplementary Fig. S6). The same broad pattern emerges: regions with the greatest increase in forest-loss exposure exhibit more negative standardised precipitation trends across most air-mass exposure windows. Across the tropics, the annual standardised contrast reaches -0.15 ± 0.005 SD yr^{-1} for 3-day exposure and remains strongly negative for 5-day exposure (-0.15 ± 0.01 SD yr^{-1}), equivalent to a study-end shift of approximately -3.6 SD. However, the regional relative response is more heterogeneous than the absolute response. Tropical America shows weak or near-zero local and 1-day relative contrasts, with stronger negative contrasts emerging only at longer windows (approx. -0.02 SD yr^{-1} for 7–10 days). Tropical Africa shows strong relative contrasts at 1–5 days (-0.15 to -0.16 SD

yr^{-1}), but weaker and more uncertain contrasts at 7–10 days. Thus, the relative analysis confirms that the tropical signal is not simply a function of baseline rainfall magnitude but is shifting outside its historical variability envelope, while also showing that the timing and strength of standardised responses vary between regions.

Seasonal analyses reveal coherent but seasonally asymmetric signals (Supplementary Figs. S7–S10). Across the tropics, regions with the greatest increase in forest-loss exposure experience substantially more negative precipitation trends in both dry and wet seasons than regions with the lowest increase in exposure. In the dry season, the strongest contrasts occur for 3–10 day back trajectories and range from -9.8 ± 0.9 to -10.1 ± 1.1 mm yr^{-1} per year, corresponding to approximately 236–243 mm lower dry-season rainfall by the end of the study period (Supplementary Fig. S7). Across tropical America, dry-season contrasts are smaller but still strengthen with multi-day exposure, reaching -7.8 ± 1.3 mm yr^{-1} per year for 5-day trajectories, or 187 ± 32 mm lower dry-season rainfall by 2024. In tropical Africa, dry-season contrasts are larger, exceeding -9 mm yr^{-1} per year across 1–10 day windows and reaching -10.1 ± 2 mm yr^{-1} per year for 3-day exposure.

Wet-season contrasts are larger still (Supplementary Fig. S9). Across the tropics, 5–10 day forest-loss exposure is associated with precipitation trends that are approximately -20 mm yr^{-1} per year more negative in the highest exposure decile, equivalent to about 484–490 mm lower wet-season rainfall by the end of the study period. Tropical Africa shows a strong and consistent wet-season response across 1–10 day windows, with contrasts of approximately -14 to -16 mm yr^{-1} per year. Tropical America also shows negative wet-season contrasts, although these are weaker and less monotonic across windows than in the annual analysis, ranging from approximately -10 to -12 mm yr^{-1} per year for 3–10 day trajectories. Relative seasonal analyses support these results: dry- and wet-season relative contrasts remain strongly negative across the tropics, particularly for multi-day exposure windows (Supplementary Figs. S8, S10). Together, these results demonstrate that the association between forest-loss exposure and declining precipitation is not confined to a single season but reflects a year-round weakening of rainfall.

Overall, increasing exposure to forest loss over 2001–2024 is associated with systematically more negative precipitation trends across regions, seasons and spatial scales. The persistence of these contrasts in both absolute and relative terms confirms that they are not driven solely by differences in mean rainfall regimes but reflect a robust and spatially coherent influence of forest loss on downwind precipitation through multi-day atmospheric pathways. Our analysis

supports a regional-transport mechanism: although local forest loss is associated with drying, the largest and most consistent contrasts emerge when upwind forest loss is accumulated along multi-day air-mass trajectories.

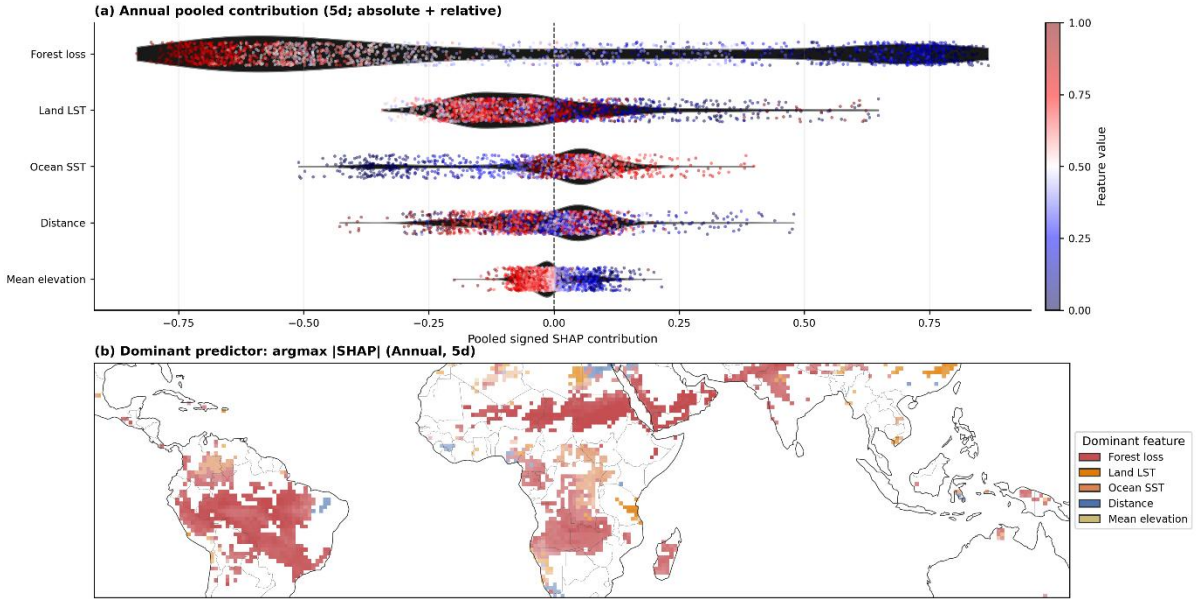


Figure 4. Machine-learning attribution of annual rainfall trends to 5-day upwind forest-loss exposure. *(a) Pooled signed SHAP contributions for the annual 5-day model, combining absolute and relative trend formulations across robust precipitation grid cells. Values are derived from an ensemble of tree-based machine learning models trained to predict grid-cell precipitation trends (2001–2024) using back-trajectory exposure metrics. Models were trained using spatial cross-validation and hyperparameter optimisation, and SHAP values were computed for each feature. Points show grid-cell contributions; colour indicates the normalised feature value representing the direction and magnitude of each feature's influence on model predictions. Violin outlines indicate the distribution density across all grid cells. (b) Spatial distribution of the dominant predictor, defined at each grid cell as the feature with the largest absolute SHAP contribution. Colours denote the dominant feature, while colour opacity scales with dominance strength, such that faded colours indicate weaker or less distinct attribution. Across both panels, features include trends in cumulative upwind forest loss exposure along air-mass trajectories, trajectory-weighted ocean surface temperature (SST) and weighted land surface temperate (LST), transport distance and mean elevation.*

Although the preceding analyses demonstrate a strong association between increasing exposure to forest loss and declining precipitation, long-term rainfall trends may reflect other aspects of air-mass history that influence moisture supply, including ocean and land surface temperatures, mean elevation along trajectories and transport distance. To assess their relative importance, we trained an ensemble of tree-based machine-learning models to predict spatial patterns of precipitation trends from corresponding trends in these trajectory-derived variables

(Methods). The models show strong predictive skill, particularly for annual robust rainfall trends, with mean training $R^2 \approx 0.92$ and testing R^2 peaking at ~0.69 for 3-day exposure windows and ~0.66 for 5-day windows, indicating substantial explanatory power while maintaining reasonable generalisation (Supplementary Fig. S11).

SHAP (SHapley Additive exPlanations) attribution identifies changes in air-mass exposure to forest loss as the largest and most consistent contributor to predicted rainfall trends (Fig. 4a). Greater exposure is associated with more negative precipitation trends, while land surface temperature (LST) and ocean surface temperature (SST) emerge as secondary but systematic predictors, alongside smaller contributions from transport distance and mean elevation. For the 5-day annual model, forest-loss exposure accounts for ~80% of the dominant-feature attribution under raw SHAP magnitudes, compared to ~10% for SST and ~7% for LST, demonstrating clear dominance even when additional thermodynamic predictors are included.

Sensitivity tests across exposure windows (1–10 days) confirm the robustness of this relationship (Supplementary Figs. S12–S15). Annual model performance peaks at intermediate integration lengths, with 3–5-day windows providing the best balance between predictive skill and generalisation (Supplementary Fig. S11), motivating the use of the 5-day configuration in Fig. 4. Seasonal behaviour is consistent with this interpretation: dry-season models favour shorter (1–3 day) pathways (Supplementary Figs. S11, S16–S20), whereas wet-season models show broader sensitivity across 3–7 days (Supplementary Figs. S11, S21–S25), consistent with stronger local land–atmosphere coupling during the dry season and more spatially distributed moisture transport during the wet season [21].

Spatial attribution identifies where individual drivers exert the strongest influence on rainfall-trend predictability. Using the feature with the largest absolute SHAP value (argmax |SHAP|) to define the dominant predictor highlights air-mass exposure to forest loss as the primary explanatory variable across extensive regions of tropical South America and Africa (Fig. 4b; Supplementary Fig. S26). Because absolute SHAP magnitudes can vary in scale among predictors, we additionally evaluated dominance using a rank-normalised metric based on each feature's percentile contribution (Supplementary Figs. S26–S28). The strong agreement between these approaches indicates that the spatial prominence of forest-loss exposure is not an artefact of scaling. Rank-normalised results also highlight a more distributed contribution from SST, LST and transport distance, but without altering the overall dominance hierarchy (Supplementary Fig. S29).

Together, these analyses show that increasing air-mass exposure to deforested landscapes provides the most consistent explanation for observed tropical precipitation trends, outweighing variability in oceanic moisture supply, land–atmosphere thermal coupling, or pathway characteristics. Although circulation adjustments may partly offset land-surface drying [30] and warming-driven moisture increases could buffer rainfall declines [31], the attribution analysis indicates that reductions in terrestrial moisture recycling associated with forest loss remain the dominant control on multi-decadal rainfall change across much of the tropics.

Our study provides robust observational evidence that increasing exposure to tropical forest loss has contributed to widespread declines in tropical precipitation. By combining satellite precipitation datasets with Lagrangian air mass back trajectories, we show that air parcels traversing increasingly deforested landscapes between 2001 and 2024 are systematically associated with more negative annual, wet-season, and dry-season precipitation trends. These relationships persist across regions and exposure windows from 1 to 10 days. Although reduced precipitation occurs directly over areas of forest loss, consistent with recent findings [3], substantially larger declines occur downwind of regions experiencing increased forest loss, demonstrating that deforestation influences rainfall both locally and through regional atmospheric transport pathways.

For 5-day back trajectories, greatest increases in exposure to forest loss resulted in annual precipitation trends of 23.8 ± 1.4 mm yr^{-1} per year more negative than regions with the smallest increases. Sustained over the 2001–2024 period regions downwind of extensive forest loss received 572 ± 33 mm less annual precipitation than regions downwind of little forest loss. Expressed relative to local interannual variability, these trends correspond to declines of ~0.15 SD yr^{-1}, implying a cumulative separation of multiple standard deviations in annual rainfall. Such a shift indicates that precipitation downwind of heavily deforested regions has moved well beyond its typical variability, reflecting a persistent reorganisation of the tropical hydrological cycle.

Machine-learning analyses further identify trends in air-mass exposure to forest loss as the strongest and most consistent predictor of long-term precipitation change, exceeding the influence of ocean surface temperature, land surface temperature, transport distance, or elevation along trajectories. While thermodynamic variables such as LST and SST contribute to rainfall variability, their influence is secondary and spatially more heterogeneous. Spatial attribution highlights large areas of South America, particularly southern Brazil and Peru, and sub-Saharan Africa where increased exposure to forest loss exerts a dominant control on

precipitation-trend predictability, underscoring the regional-scale hydrological consequences of land-use change.

Our findings suggest that reducing deforestation would provide substantial benefits for regional rainfall, alongside climate mitigation and biodiversity conservation. Climate change and plant physiological responses to elevated carbon dioxide may further exacerbate impacts on regional hydrology, with large reductions in precipitation projected for the Amazon[32,33]. The sensitivity of precipitation to upwind forest-loss transport pathways, equivalent to atmospheric distances of hundreds to thousands of kilometres, highlights the need for coordinated regional land-use planning and transboundary governance [34].

Ultimately, these results reveal a critical feedback between tropical land-cover change and atmospheric moisture availability: continued forest loss weakens regional moisture recycling, amplifies drying trends, and undermines the stability and resilience of tropical precipitation regimes.

Methods

Back-trajectory model

Daily atmospheric back-trajectories were calculated using the Reading Offline TRAJectory model (ROTRAJ) [35]. ROTRAJ computes air-parcel positions using meteorological fields from ECMWF ERA5 reanalysis [36] with cubic Lagrange interpolation in the vertical, bilinear interpolation in the horizontal, and linear interpolation in time. Trajectory positions were integrated at 30-minute intervals and archived every 3 hours. In total, we computed approximately 600 million 10-day back-trajectories, arriving at 6-hourly intervals each day (00:00, 06:00, 12:00 and 18:00 UTC) at the centre of every 1 degree x 1 degree grid cell across the tropical domain (30 °N to 30 °S) from 1 January 2001 to 31 December 2024. For each grid cell, trajectories were simulated at three vertical levels defined in sigma-pressure coordinates: near-surface (sigma = 0.99) and higher atmospheric layers at sigma = 0.9 and sigma = 0.8.

Land-use data

Forest cover and forest cover loss were obtained from the Global Forest Change (GFC) dataset [37], version 1.12, which provides global forest extent and change from 2000 to 2024 at 1 arc-second resolution. Forest cover in 2000 is defined as the percentage canopy closure for vegetation taller than 5 m. Annual forest-loss layers from 2001 to 2024 were combined with the 2000 forest cover layer to construct a time-varying land-surface dataset. To integrate these data with the coarser trajectory-analysis grid, forest cover and annual forest-loss layers were aggregated to 1 ° x 1 ° resolution. Annual forest-loss fields were then linearly interpolated in time to generate monthly, and subsequently daily, gridded fields for trajectory sampling.

Elevation data

Elevation data were obtained from the Global Multi-resolution Terrain Elevation Data 2010 (GMTED2010) dataset [38] and resampled to 1 ° x 1 ° analysis grid using mean aggregation. These fields were used to quantify the mean, median and maximum elevation encountered along each trajectory pathway.

Precipitation data

There is substantial uncertainty in rainfall trends across the tropics [3], including over the Amazon (Polasky et al., 2025; Sapucci et al., 2022). To reduce dependence on any single retrieval algorithm, we used an ensemble of six daily precipitation products, following previous multi-product approaches [3,41]: (1) CHIRPS v2 [42], (2) CMORPH CDR v1 [43], (3) PERSIANN-CDR v1

Revision 1 [44], (4) IMERG v7 [45], (5) GPCP CDR v1.3 [46], and (6) PERSIANN-CCS-CDR [47]. Daily precipitation from each product for 2001-2024 was regridded to the 1 ° x 1 ° grid using bilinear interpolation.

We then constructed a daily ensemble precipitation dataset by averaging across the six products at each grid cell. Seasonal rainfall metrics were defined using an adapted version of [NO_PRINTED_FORM] [12]. For each grid cell and year, months were ranked by total precipitation. The three wettest months were classified as the wet season, the three driest months as the dry season. Seasonal precipitation totals were then computed consistently across all datasets.

Across the six precipitation datasets analysed in this study, the total annual, dry season, and wet season trends for the period 2001–2024 exhibit substantial variability in both sign and magnitude (Supplementary Figures S30–S32). Nevertheless, when the individual dataset trends are stacked and ranked according to their agreement in trend direction, coherent regions of sign-level consensus emerge, particularly over large portions of South America and Africa (Supplementary Figures S33–S35). To address discrepancies in trend magnitude among datasets, we generated ensemble rainfall trends using two aggregation approaches: (1) an arithmetic mean, computed as the per-grid-cell sum of all six precipitation products divided by the number of datasets, and (2) a median aggregation, defined as the per-grid-cell median value across the six datasets. Differences in computed trends between these two ensemble methods are minimal across seasons thus, all results presented in this study are based on trends derived from the arithmetic-mean ensemble.

Air-mass back-trajectory exposure metrics

Atmospheric moisture-source and land-surface exposure were quantified from the 10-day backward trajectories. Each trajectory consists of parcel locations archived every 3 hours over 240 hours upstream of the arrival point. For each grid cell and day, four trajectories were calculated (00, 06, 12, and 18 UTC arrivals), and exposure metrics were computed separately for each trajectory and then averaged across the four 6-hourly trajectories to produce a daily estimate of upstream air-mass history.

All exposure metrics were calculated for five nested upstream time windows: 1, 3, 5, 7, and 10 days preceding arrival. This allowed us to test the sensitivity of precipitation-rainfall relationships to different transport timescales.

Ocean exposure

For each trajectory step, we classified the parcel location as land or ocean using a land-sea mask. Ocean-related exposure metrics were then calculated over ocean segments of the trajectory only. Sea surface temperature (SST) was sampled along the trajectory path using ERA5 SST fields at the nearest grid point in space and time. For each exposure window, we calculated the mean SST encountered over ocean segments (sst_ocean), and an SST metric with ocean gaps infilled where necessary (sst_ocean_filled), together with the fraction of trajectory time spent over ocean (ocean_frac) and an indicator of whether ocean was encountered within the window (has_ocean).

Land-surface exposure

Land-surface properties were sampled along each trajectory using the gridded forest cover, forest loss and elevation fields. For each window, and restricting calculations to land segments where appropriate, we computed the cumulative forest loss and cover exposure encountered over the trajectory pathway. Exposure trends to forest loss and forest cover are broadly similar, with increasing loss exposure generally corresponding to declining cover exposure across regions and windows (Supplementary Fig. S36). This is expected because both reflect the same underlying land-cover change along air-mass pathways. However, forest loss more directly captures recent disturbance, whereas forest cover represents the broader vegetation background state. Cumulative forest loss exposure therefore represents the integrated deforestation signal encountered by an air mass during transport, capturing both the intensity and duration of exposure along its pathway. We therefore focus on forest loss exposure in the main analysis.

We also calculated residence time over land and ocean and their fractional equivalents. Land surface temperature was sampled along the trajectory path using ERA5 skin temperature fields at the nearest grid point in space and time.

Terrain and trajectory geometry

To characterise the physical pathways of air masses, we calculated summary elevation metrics along each trajectory window (elevation_mean, elevation_median, elevation_max) and two geometric transport distance metrics: cumulative path length travelled by the parcel (traj_pathlen_km) and straight-line displacement between the arrival point and the upwind endpoint (traj_displacement_km). These variables quantify both the terrain crossed by the air mass and the scale and geometry of transport.

Trajectory thermodynamics

We also extracted thermodynamic state variables directly from the trajectory output, including specific humidity, air temperature, pressure and potential vorticity. For each exposure window, we calculated summary statistics of specific humidity and temperature, including mean, standard deviation, 10th percentile, 90th percentile, total change across the window, and linear slope through time. We also calculated relative humidity, mean moisture deficit, and surface moisture-deficit diagnostics derived from parcel temperature, pressure and humidity. These variables were used to characterize the moisture content and moisture-uptake potential of the air mass during transport. In the machine-learning analysis, however, we excluded these trajectory thermodynamic variables in order to focus attribution on land and ocean exposure metrics rather than the internal thermodynamic state of the parcel itself.

Sensitivity to trajectory height

To test whether the inferred exposure patterns depended on the level at which trajectories were initiated, we repeated the exposure calculations for sigma = 0.99, 0.9 and 0.8. Exposure fields were highly similar across these levels, indicating that the principal exposure gradients are not artefacts of trajectory height. Accordingly, all results shown in the main text are based on near-surface trajectories (sigma = 0.99).

Trend calculation

Seasonal and annual metrics

For each grid cell and each variable, we first constructed annual, dry-season and wet-season time series over 2001-2024. For precipitation, annual totals and seasonal totals were calculated from the ensemble daily precipitation series. For trajectory-derived exposure variables, daily exposure fields were aggregated to annual, dry-season and wet-season means so that precipitation and exposure trends were computed over consistent temporal definitions.

Trend estimation

For each grid cell and variable, we estimated long-term trends over 2001-2024 using a bootstrap-based slope framework. Trends were computed both in native physical units and in standardized relative units. For the standardized version, each time series was converted to a z-score by subtracting the mean and dividing by the standard deviation, yielding trends in units of standard deviations per year (SD yr^{-1}). Standardization allowed comparison across variables and climatic regions with different absolute variability, while raw trends retained direct physical interpretability.

We then generated 1,000 bootstrap resamples of each time series with replacement, preserving the original time values associated with each sampled observation. For each bootstrap sample, we fitted a linear trend and stored the resulting slope. From the distribution of bootstrap slopes, we extracted the median slope as the trend estimate and the 2.5th and 97.5th percentiles as the 95% confidence interval.

Robust trend classification

We classified a trend as robust when two conditions were met: (1) the 95% confidence interval did not cross zero, and (2) the confidence-interval width was less than twice the absolute slope magnitude. This second criterion ensured that robust trends were not only different from zero but also sufficiently constrained relative to their estimated magnitude. Each trend NetCDF therefore contains both the median slope field and a corresponding binary robustness classification (robust_combined).

Native absolute and standardized trend representations

We retained both raw and standardized trends throughout the analysis. For precipitation, raw trends are expressed in mm yr^{-1} per year, whereas standardized trends express the rate of change relative to local variability in units of SD yr^{-1}. For trajectory exposure metrics, raw trends preserve physical meaning, whereas standardized trends reduce the influence of baseline magnitude and heteroscedasticity across regions. We therefore used both representations in the our analysis to assess robustness to scaling and to separate physical interpretability from scale-independent pattern detection.

Climate-mode adjusted precipitation trends

To assess the extent to which precipitation trends may reflect large-scale climate variability, we also calculated climate-mode-adjusted precipitation trends. Annual precipitation totals were regressed against time while including standardized annual means of three major tropical SST mode indices as covariates: Niño-3.4 for El Niño–Southern Oscillation (ENSO), the Dipole Mode Index for the Indian Ocean Dipole (IOD), and ATL3 for Atlantic Niño variability. Monthly index values were obtained from NOAA products and aggregated to annual means for consistency with the precipitation analysis. These adjusted trends are used as a sensitivity test rather than as the primary analysis, allowing us to assess whether observed relationships are robust to large-scale climate variability. We find that climate mode–adjusted precipitation trends closely mirror the observed trends in both spatial pattern and magnitude (Supplementary Fig. S4), indicating that the observed drying signals are not dominated by large-scale climate modes

such as ENSO, the Indian Ocean IOD or ATL3. Thus, the main results presented here uses raw precipitation trends in both native absolute and standardized form.

Exposure-decile analysis

To evaluate how increasing exposure to forest loss relates to long-term rainfall change, grid cells were grouped into ten equal-sized deciles according to their trends in air-mass exposure to forest loss. For each decile, we examined the distribution of precipitation trends and compared the lowest and highest exposure categories. Differences between the first and tenth deciles were assessed using a set of complementary statistical tests: Kolmogorov-Smirnov [48], Mann-Whitney U [49], Anderson-Darling k-sample [50], Welch's t-test on log-transformed data [51], and Wasserstein distance [52]. We considered the contrast between the highest and lowest deciles to be statistically meaningful when at least three of the five tests indicated $p < 0.05$, or where the Wasserstein distance indicated substantial distributional separation. We additionally quantified differences in mean precipitation trends between the tenth and first deciles using 5,000 bootstrap resamples, reporting the 2.5th and 97.5th percentiles as 95% confidence intervals.

Machine-learning modelling and feature attribution

Objective and predictor set

Our machine-learning analysis was designed to evaluate whether trends in air-mass exposure to forest loss remain important relative to other trajectory-derived predictors of rainfall change. Models were therefore used to assess the relative explanatory power of competing predictors rather than to infer causality.

The response variable was the precipitation trend at each grid cell, analysed separately for annual, dry-season and wet-season rainfall. All models were trained and evaluated exclusively on robust precipitation grid cells, defined using the bootstrap-based robustness criteria described above (Methods). We trained models for both absolute and standardised precipitation trends.

Predictors were restricted to trajectory-derived exposure metrics. These included trends in cumulative upwind forest-loss exposure, trajectory-weighted ocean surface temperature (SST), trajectory-weighted land surface temperature (LST), transport distance, and mean elevation along air-mass pathways. Land and ocean residence metrics were considered during model selection but were not consistently retained in best-performing configurations.

Model classes and tuning

We trained an ensemble of tree-based regression models, including Random Forest, Extra Trees, XGBoost and CatBoost where available. For each combination of season and exposure window, models were tuned using RandomizedSearchCV over model-specific hyperparameter distributions.

To avoid inflation of predictive skill due to spatial autocorrelation, both hyperparameter tuning and model evaluation used grouped spatial cross-validation. Grid cells were partitioned into geographically contiguous blocks; subsets of these blocks were withheld for testing, while the remaining blocks were used for training and cross-validation. This spatial blocking provides a conservative estimate of model skill and better reflects generalisation to independent regions.

Ensemble prediction

For each model family, the best-performing estimator (based on cross-validated R^2) was retained. Ensemble predictions were computed as a weighted mean of model-specific predictions, with weights proportional to cross-validated performance:

$$w_m \frac{max(CV\ R_m^2, 0.01)}{\sum_j max\left(CV\ R_j^2, 0.01\right)}$$

where m indexes the candidate model families. The floor of 0.01 prevented any model from receiving zero weight while still allowing higher-performing models to contribute more strongly. Ensemble performance was then evaluated using training and held-out test predictions.

Performance metrics and model selection

For each ensemble configuration we computed training and test R^2, RMSE, MAE, Spearman correlation, and the train–test R^2 gap. Model evaluation emphasised both predictive skill and generalisation, with particular focus on test R^2 and the train–test gap as complementary diagnostics.

Exposure-window sensitivity was assessed by comparing model performance across 1–10 day trajectory lengths. Rather than selecting a single optimal window, we identified exposure lengths that consistently combine high predictive skill with moderate train–test gaps. Intermediate windows (typically 3–5 days) provide the most robust balance and are therefore used for pooled attribution analyses in the main figures.

SHAP attribution

To interpret the fitted models, we computed SHAP values using TreeExplainer [53] for each tuned model. Because raw SHAP magnitudes differ across models and feature sets, we converted

each grid cell's SHAP vector to a signed fractional contribution by dividing each feature-specific SHAP value by the sum of absolute SHAP values across all features for that cell:

$$SignedShare_{i,f} = \frac{SHAP_{i,f}}{\sum_k |SHAP_{i,k}|}$$

where i indexes grid cells and f indexes features. This yields a signed quantity bounded by -1 and 1 that describes the direction and relative contribution of each predictor to the local model output.

Pooling SHAP across model families

For each modelling configuration, signed fractional SHAP contributions were pooled across model families using the same ensemble weights used for prediction:

$$PooledShare_{i,f} = \sum_m w_m \times SignedShare_{i,f,m}$$

This produces a single ensemble-weighted attribution field for each predictor and grid cell. Mean absolute pooled contributions were used to rank predictors globally, while the predictor with the largest absolute pooled contribution (argmax |SHAP|) at each grid cell was defined as the locally dominant feature.

To account for differences in feature variance, we additionally computed rank-normalised SHAP contributions by transforming absolute SHAP magnitudes to percentile ranks prior to dominance classification. This provides a scale-independent comparison of predictor importance.

Feature-selection summaries

To assess the consistency of predictor importance, we summarised feature selection across ensemble models and exposure windows, identifying predictors that are consistently retained across seasons.

Software

All analyses were conducted in Python, using xarray, numpy, pandas, scikit-learn, xgboost, catboost, shap, matplotlib, cartopy, rasterio, geopandas, and related geospatial and scientific computing libraries.

Acknowledgements

This study was supported by the São Paulo Research Foundation (FAPESP), Brazil. Process Number 2025/02016-9, UK Research and Innovation (grant ref: EP/Y030222/1) and the International Science Partnerships Fund (ISPF), through the Met Office Climate Science for Service Partnership Brazil.

Ethics declarations

The authors declare no competing interests.

References

1. Alkama, R. & Cescatti, A. Biophysical climate impacts of recent changes in global forest cover. *Science (1979)*. 351, 600–604 (2016).

2. Butt, E. W. *et al*. Amazon deforestation causes strong regional warming. *Proc. Natl. Acad. Sci. U. S. A*. 120, e2309123120 (2023).

3. Smith, C., Baker, J. C. A. & Spracklen, D. V. Tropical deforestation causes large reductions in observed precipitation. *Nature* 615, 270–275 (2023).

4. Parsons, L. A. *et al*. Tropical deforestation accelerates local warming and loss of safe outdoor working hours. *One Earth* 4, 1730–1740 (2021).

5. Reddington, C. *et al*. Tropical deforestation causes considerable heat-related mortality. Preprint at https://doi.org/10.21203/rs.3.rs-5664782/v1 (2025).

6. Leite-Filho, A. T., Soares-Filho, B. S., Davis, J. L., Abrahão, G. M. & Börner, J. Deforestation reduces rainfall and agricultural revenues in the Brazilian Amazon. *Nat. Commun*. 12, 2591 (2021).

7. Spera, S. A., Galford, G. L., Coe, M. T., Macedo, M. N. & Mustard, J. F. Land-use change affects water recycling in Brazil's last agricultural frontier. *Glob. Chang. Biol*. 22, 3405–3413 (2016).

8. Hubau, W. *et al*. Asynchronous carbon sink saturation in African and Amazonian tropical forests. *Nature* 579, 80–87 (2020).

9. Gatti, L. V. *et al*. Amazonia as a carbon source linked to deforestation and climate change. *Nature* 595, 388–393 (2021).

10. Stickler, C. M. *et al*. Dependence of hydropower energy generation on forests in the Amazon Basin at local and regional scales. *Proceedings of the National Academy of Sciences* 110, 9601–9606 (2013).

11. Marengo, J. A. *et al*. Extreme Drought in the Brazilian Pantanal in 2019–2020: Characterization, Causes, and Impacts. *Frontiers in Water* 3, (2021).

12. Spracklen, D. V., Arnold, S. R. & Taylor, C. M. Observations of increased tropical rainfall preceded by air passage over forests. *Nature* 489, 282–285 (2012).

13. Baker, J. C. A. & Spracklen, D. V. Divergent Representation of Precipitation Recycling in the Amazon and the Congo in CMIP6 Models. *Geophys. Res. Lett*. 49, (2022).

14. Dominguez, F. *et al*. Amazonian Moisture Recycling Revisited Using WRF With Water Vapor Tracers. *Journal of Geophysical Research: Atmospheres* 127, (2022).

15. Van Der Ent, R. J., Savenije, H. H. G., Schaefli, B. & Steele-Dunne, S. C. Origin and fate of atmospheric moisture over continents. *Water Resour. Res*. 46, (2010).

16. Staal, A. *et al*. Forest-rainfall cascades buffer against drought across the Amazon. *Nature Climate Change 2018 8:6* 8, 539–543 (2018).

17. Zemp, D. C. *et al*. On the importance of cascading moisture recycling in South America. *Atmos. Chem. Phys*. 14, 13337–13359 (2014).

18. Smith, C. *et al.* Observed and simulated local climate responses to tropical deforestation. *Environmental Research Letters* 18, 104004 (2023).

19. Luo, X. *et al.* The Biophysical Impacts of Deforestation on Precipitation: Results from the CMIP6 Model Intercomparison. *J. Clim.* 35, 3293–3311 (2022).

20. Spracklen, D. V. & Garcia-Carreras, L. The impact of Amazonian deforestation on Amazon basin rainfall. *Geophys. Res. Lett.* 42, 9546–9552 (2015).

21. Qin, Y., Wang, D., Ziegler, A. D., Fu, B. & Zeng, Z. Impact of Amazonian deforestation on precipitation reverses between seasons. *Nature* 639, 102–108 (2025).

22. Silveira, M. V. F. *et al.* Observed shifts in regional climate linked to Amazon deforestation. *Commun. Earth Environ.* 6, 948 (2025).

23. Franco, M. A. *et al.* How climate change and deforestation interact in the transformation of the Amazon rainforest. *Nat. Commun.* 16, 7944 (2025).

24. Gu, G. & Adler, R. F. Observed variability and trends in global precipitation during 1979–2020. *Clim. Dyn.* 61, 131–150 (2023).

25. Gu, G., Adler, R. F. & Huffman, G. J. Long-term changes/trends in surface temperature and precipitation during the satellite era (1979–2012). *Clim. Dyn.* 46, 1091–1105 (2016).

26. Fu, R. *et al.* Increased dry-season length over southern Amazonia in recent decades and its implication for future climate projection. *Proceedings of the National Academy of Sciences* 110, 18110–18115 (2013).

27. Fu, Y. & Wu, Q. Recent Emerging Shifts in Precipitation Intensity and Frequency in the Global Tropics Observed by Satellite Precipitation Data Sets. *Geophys. Res. Lett.* 51, (2024).

28. Jiang, Y. *et al.* Widespread increase of boreal summer dry season length over the Congo rainforest. *Nat. Clim. Chang.* 9, 617–622 (2019).

29. Raghavendra, A. *et al.* The MJO's impact on rainfall trends over the Congo rainforest. *Clim. Dyn.* 54, 2683–2695 (2020).

30. Liu, Y. *et al.* Recent Forest Loss in the Brazilian Amazon Causes Substantial Reductions in Dry Season Precipitation. *AGU Advances* 6, (2025).

31. Laipelt, L. *et al.* Increased Amazon evapotranspiration since 1990 in a warming climate. *Environmental Research Letters* 20, 104025 (2025).

32. Ruv Lemes, M. *et al.* Impacts on South America moisture transport under Amazon deforestation and 2 °C global warming. *Science of The Total Environment* 905, 167407 (2023).

33. Sampaio, G. *et al.* CO_2 physiological effect can cause rainfall decrease as strong as large-scale deforestation in the Amazon. *Biogeosciences* 18, 2511–2525 (2021).

34. Keys, P. W., Wang-Erlandsson, L., Gordon, L. J., Galaz, V. & Ebbesson, J. Approaching moisture recycling governance. *Global Environmental Change* 45, 15–23 (2017).

35. Methven, J. *et al.* Estimating photochemically produced ozone throughout a domain using flight data and a Lagrangian model. *Journal of Geophysical Research: Atmospheres* 108, (2003).

36. Hersbach, H. *et al.* The ERA5 global reanalysis. *Quarterly Journal of the Royal Meteorological Society* 146, 1999–2049 (2020).

37. Hansen, M. C. *et al.* High-Resolution Global Maps of 21st-Century Forest Cover Change. *Science (1979).* 342, 850–853 (2013).

38. Danielson, J. J. & Gesch, D. B. *Global Multi-Resolution Terrain Elevation Data 2010 (GMTED2010)*. (2011) doi:10.3133/ofr20111073.

39. Polasky, A., Sapkota, V., Forest, C. E. & Fuentes, J. D. Discrepancies in precipitation trends between observational and reanalysis datasets in the Amazon Basin. *Sci. Rep.* 15, 7268 (2025).

40. Sapucci, C. R., Mayta, V. C. & da Silva Dias, P. L. Evaluation of diverse-based precipitation data over the Amazon Region. *Theor. Appl. Climatol.* 149, 1167–1193 (2022).

41. Xu, H. *et al.* Rising ecosystem water demand exacerbates the lengthening of tropical dry seasons. *Nat. Commun.* 13, 4093 (2022).

42. Funk, C. C. *et al. A Quasi-Global Precipitation Time Series for Drought Monitoring*. https://data.chc.ucsb.edu/products/CHIRPS-2.0/global_daily/netcdf/p25 (2014) doi:10.3133/ds832.

43. Xie, P. *et al.* NOAA Climate Data Record (CDR) of CPC Morphing Technique (CMORPH) High Resolution Global Precipitation Estimates, Version 1. NOAA National Centers for Environmental Information. https://doi.org/https://doi.org/10.25921/w9va-q159 (2019) doi:https://doi.org/10.25921/w9va-q159.

44. Sorooshian, S., Hsu, K., Braithwaite, D., Ashouri, H. & NOAA CDR Program. NOAA Climate Data Record (CDR) of Precipitation Estimation from Remotely Sensed Information using Artificial Neural Networks (PERSIANN-CDR), Version 1 Revision 1. NOAA National Centers for Environmental Information. Preprint at https://doi.org/doi:10.7289/V51V5BWQ (2014).

45. Huffman, G. *et al.* Integrated Multi-satellitE Retrievals for GPM (IMERG) Version 07. NASA's Precipitation Processing Center. https://gpm1.gesdisc.eosdis.nasa.gov/data/GPM_L3/GPM_3IMERGDF.07/ (2023).

46. Huffman, G. J. *et al.* Global Precipitation at One-Degree Daily Resolution from Multisatellite Observations. *J. Hydrometeorol.* 2, 36–50 (2001).

47. Sadeghi, M. *et al.* PERSIANN-CCS-CDR, a 3-hourly 0.04° global precipitation climate data record for heavy precipitation studies. *Sci. Data* 8, 157 (2021).

48. Massey, F. J. The Kolmogorov-Smirnov Test for Goodness of Fit. *ournal of the American Statistical Association* 46, 68–78 (1951).

49. Mann, H. B. & Whitney, D. R. On a Test of Whether One of Two Random Variables is Stochastically Larger than the Other. *The Annals of Mathematical Statistics* 18, 50–60 (1947).

50. Scholz, F. W. & Stephens, M. A. K-sample Anderson–Darling Tests. *Journal of the American Statistical Association* 82, 918–924 (1987).

51. Welch, B. L. The Generalization of 'Student's' Problem When Several Different Population Variances are Involved. *Biometrika* 34, 28–35 (1947).

52. Levina, E. & Bickel, P. The Earth Mover's distance is the Mallows distance: some insights from statistics. in *Proceedings Eighth IEEE International Conference on Computer Vision*. *ICCV 2001* 251–256 (IEEE Comput. Soc, 2001). doi:10.1109/ICCV.2001.937632.

53. Lundberg, S. & Lee, S.-I. A Unified Approach to Interpreting Model Predictions. (2017).

Supplementary Files

This is a list of supplementary files associated with this preprint. Click to download.

- TrajforestlossprecipSupplementaryFigs2026.docx